Journal of Geodynamics 113 (2018) 1–12

Contents lists available at ScienceDirect

Journal of Geodynamics

journal homepage: www.elsevier.com/locate/jog

Flexural modeling of the elastic lithosphere at an ocean trench: A parameter sensitivity analysis using analytical solutions

Eduardo Contreras-Reyes*, Jeremías Garay

Departamento de Geofísica, Facultad de Ciencias Físicas y Matemáticas, Universidad de Chile, Santiago, Chile

ARTICLE INFO

Keywords:
Flexure
Oceanic lithosphere
Elastic thickness
Angle of subduction
Bending moment

ABSTRACT

The outer rise is a topographic bulge seaward of the trench at a subduction zone that is caused by bending and flexure of the oceanic lithosphere as subduction commences. The classic model of the flexure of oceanic lithosphere $w(x)$ is a hydrostatic restoring force acting upon an elastic plate at the trench axis. The governing parameters are elastic thickness T_e, shear force V_0, and bending moment M_0. V_0 and M_0 are unknown variables that are typically replaced by other quantities such as the height of the fore-bulge, w_b, and the half-width of the fore-bulge, $(x_b - x_o)$. However, this method is difficult to implement with the presence of excessive topographic noise around the bulge of the outer rise. Here, we present an alternative method to the classic model, in which lithospheric flexure $w(x)$ is a function of the flexure at the trench axis w_0, the initial dip angle of subduction β_0, and the elastic thickness T_e. In this investigation, we apply a sensitivity analysis to both methods in order to determine the impact of the differing parameters on the solution, $w(x)$. The parametric sensitivity analysis suggests that stable solutions for the alternative approach requires relatively low β_0 values ($< 15^\circ$), which are consistent with the initial dip angles observed in seismic velocity-depth models across convergent margins worldwide. The predicted flexure for both methods are compared with observed bathymetric profiles across the Izu-Mariana trench, where the old and cold Pacific plate is characterized by a pronounced outer rise bulge. The alternative method is a more suitable approach, assuming that accurate geometric information at the trench axis (i.e., w_0 and β_0) is available.

1. Introduction

Slab pull is one of the most important forces driving plate tectonics and continental drift (e.g., Forsyth and Uyeda, 1975; Conrad and Lithgow-Bertelloni, 2002). It is associated with the negative buoyancy of the dense, cold rocks of the sinking oceanic lithosphere. Due to the stiffness of the lithosphere and its elastic behavior at long wavelengths (several hundred kilometers), it can transmit stresses efficiently to the surface and is able to pull the lower plate toward the ocean trench. A consequence of this process is the bending of the oceanic plate prior to subduction, which is characterized by the formation of a prominent fore-bulge (the outer rise). Modeling the flexural bending of the oceanic lithosphere provides important constraints on trench tectonic loading and on the long term strength of the lithosphere (e.g., Bodine et al., 1981; Mueller and Phillips, 1995; Capitanio et al., 2009). Additionally, as the flexural curvature becomes significant, bending stresses could exceed the yield strength of the lithosphere (e.g., McNutt and Menard, 1982), causing pervasive faulting and tensional earthquakes in the upper part of the oceanic plate (Christensen and Ruff, 1988; Masson, 1991; Ruiz and Contreras-Reyes, 2015), as well as local plate weakening (e.g., Turcotte et al., 1978; Bodine and Watts, 1979; McAdoo et al., 1985; Judge and McNutt, 1991; Levitt and Sandwell, 1995; Watts, 2001; Billen and Gurnis, 2005; Contreras-Reyes and Osses, 2010; Zhang et al., 2014).

The flexural wavelength and amplitude of the outer rise has been modeled using an elastic lithosphere overlying a weak astenosphere. In this model, the lithosphere is loaded on the arcward side of the trench axis by a shear force V_0 and bending moment M_0 (Fig. 1A; Watts and Talwani, 1974; Parsons and Molnar, 1978; Levitt and Sandwell, 1995; Bry and White, 2007; Contreras-Reyes and Osses, 2010; Zhang et al., 2014; Hunter and Watts, 2016). The third independent parameter is the elastic thickness T_e, which in turn is related to the flexural rigidity $D = \frac{ET_e^3}{12(1-\nu^2)}$; a measure of the flexural resistance to loading. The Young's modulus, E, and Poisson's ratio, ν, are material properties commonly treated as constants. With this assumption, strong plates have large elastic thickness T_e, while weak plates have small elastic thickness T_e. Thereby, the independent three parameters V_0, M_0 and T_e have been classically used to model the flexure of the oceanic

* Corresponding author.
E-mail address: econtreras@dgf.uchile.cl (E. Contreras-Reyes).

https://doi.org/10.1016/j.jog.2017.11.004
Received 11 July 2017; Received in revised form 23 October 2017; Accepted 7 November 2017
Available online 10 November 2017

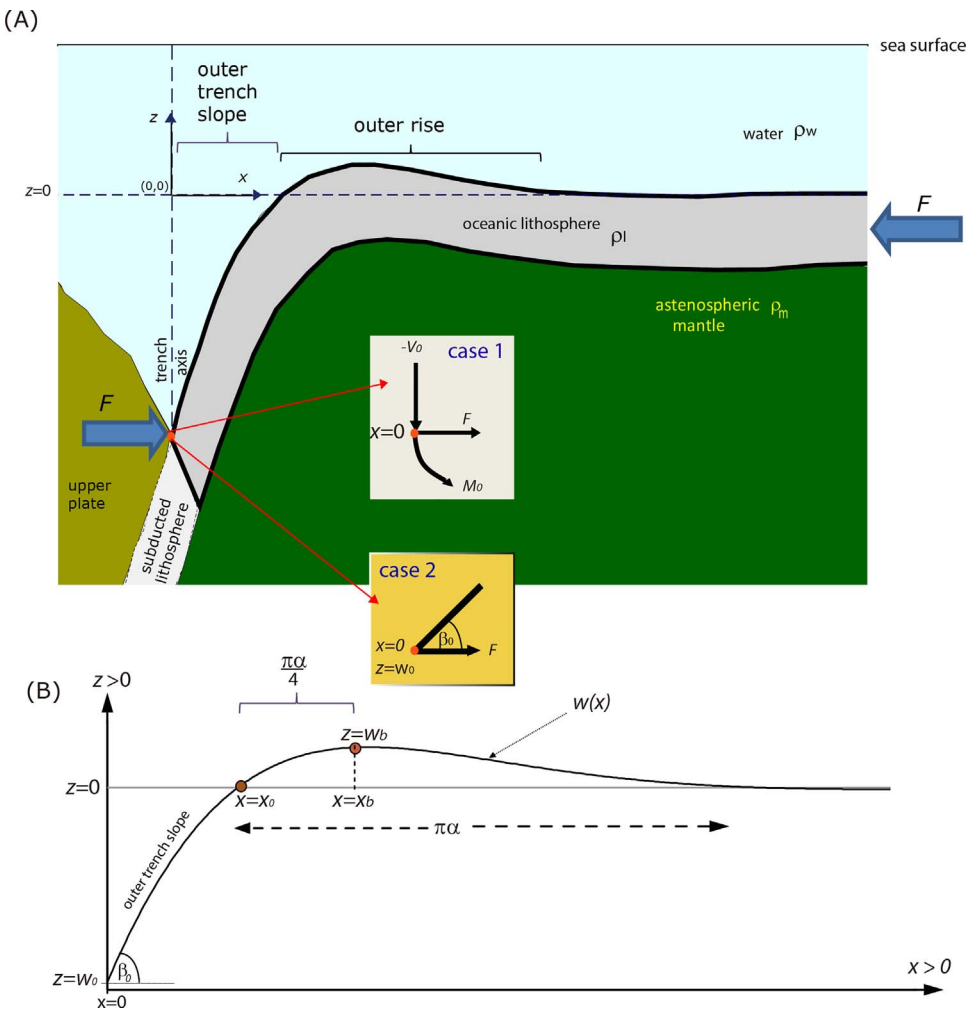

Fig. 1. (A) Bending of the lithosphere at an ocean trench due to the applied vertical shear force V_0, horizontal force F and bending moment M_o. ρ_m, ρ_l, and ρ_w are the astenospheric mantle, lithosphere and water density, respectively. (B) Schematic representation of topography (x_o, x_b, w_b, α) defining the deflection curve $w(x)$. The point (x_b, w_b) corresponds to the position of the maximum positive amplitude of $w(x)$ or peak of the outer rise while (0, w_0) corresponds to the position of the maximum negative amplitude of $w(x)$ at the trench axis. β_0 is the initial angle of subduction at the trench axis and it is related to $w(x)$ as $\tan\beta_0 = dw/dx|_{x=0}$.

lithosphere using an elastic rheology. However, V_0 and M_0 cannot be determined directly, whereas other quantities can be measured from bathymetric profiles, such as the amplitude of the fore-bulge w_b and the half-width of the fore-bulge $x_b - x_o$ (Fig. 1B), and are typically used in the classic approach to model the shape of the outer rise (Caldwell et al., 1976; Turcotte and Schubert, 2002). In practice, however, these morphological quantities present considerable uncertainties associated with bathymetric noise and are hardly recognizable along some profiles inhibiting the constraint of lithospheric parameters. In this paper, we present an alternative approach to analytically model the flexure of the oceanic lithosphere using, as independent parameters, the flexure at the trench axis w_0 (depth of the trench axis), the initial dip angle of subduction at the trench axis β_0, and the elastic thickness T_e. w_0 and β_0 are quantities that can be directly measured from bathymetric profiles across poorly sediment-loaded trenches, which occur in more than 50% of the convergent margins (von Huene and Scholl, 1991). A comparison between the classical method and the new approach is presented in two steps. First, we present a parametric sensitivity analysis using the analytical solutions for the predicted lithospheric flexure associated with each approach. Second, we model the shape of the outer rise across the Izu-Marianas trench where the outer rise of the older oceanic Pacific plate is well developed. Advantages and disadvantages, as well as tectonic implications, of both methods are discussed in the following.

2. Flexural modelling

The flexure of the oceanic lithosphere at trenches is modeled as a hydrostatic restoring force $g(\rho_m - \rho_w)w$ acting upon an elastic plate, where w is plate flexure, g is average gravity, and ρ_m and ρ_w are mantle and water density, respectively (Fig. 1; Caldwell et al., 1976; Levitt and Sandwell, 1995; Turcotte and Schubert, 2002; Bry and White, 2007; Contreras-Reyes and Osses, 2010; Hunter and Watts, 2016). If the applied load implements a horizontal force F, and a bending moment M, the deflection w of the plate is governed by the following differential equation:

$$-\frac{d^2M}{dx^2} + \frac{d}{dx}\left(F\frac{dw}{dx}\right) + \Delta\rho g = q(x) \tag{1}$$

where $q(x)$ is the vertical load acting on the plate, and $\Delta\rho = \rho_m - \rho_w$ is the density contrast between the asthenospheric mantle ρ_m and sea water ρ_w (Fig. 1). The bending moment M and the shear force V are related to the negative curvature of the plate $\kappa = -d^2w/dx^2$, by the flexural rigidity D:

$$M(x) = -D\frac{d^2w}{dx^2} \tag{2}$$

and

$$V(x) = \frac{dM}{dx} - F\frac{dw}{dx} \tag{3}$$

Combining these three equations, and assuming F = cte and $q = 0$ we have:

$$D\frac{d^4w}{dx^4} + F\frac{d^2w}{dx^2} + \Delta\rho g = 0 \tag{4}$$

The general solution of (4) which considers the boundary condition

Table 1
Values of parameters and constants used in flexural modeling.

Name	Symbol	Value	Unit
Young's modulus	E	70×10^9	Pa
Acceleration due to gravity	g	9.81	m s^{-2}
Poisson's ratio	ν	0.25	
Mantle density	ρ_m	3300	kg m^{-3}
Water density	ρ_w	1030	kg m^{-3}

of no flexure away from the load (i.e., $w \to 0$ as $x \to \infty$) is given by:

$$w(x) = e^{-\eta\frac{x}{\alpha}}\left[C_1\cos\left(\xi\frac{x}{\alpha}\right) + C_2\sin\left(\xi\frac{x}{\alpha}\right)\right] \quad (5)$$

where $\alpha = (4D/\Delta\rho g)^{1/4}$ is the flexural parameter that defines the natural wavelength of the elastic lithosphere (the more rigid the lithosphere, the longer the wavelength of the bulge). In addition, $\eta = \sqrt{1-\gamma}$ and $\xi = \sqrt{1+\gamma}$, where $\gamma = \frac{F}{(4Dg\Delta\rho)^{1/2}} = \frac{F}{F_c}$, is the dimensionless force. F_c corresponds to the minimum force by which the lithosphere will become unstable and take a sinusoidal shape, eventually causing the plate to buckle (Turcotte and Schubert, 2002). Parsons and Molnar (1978) conclude that even a large horizontal load F will not have a considerable effect on the deformation of the plate, and F cannot be precisely determined from bathymetric profiles. The compressional critical stress associated with F_c can be calculated as $\sigma_c = \sqrt{\frac{ET_e\Delta\rho g}{3(1-\nu^2)}}$, from which, using typical values shown in Table 1the reference $T_e = 50$ km, we conclude that σ_c is approximately 5 GPa. Due to the substantial stress requirement, we conclude that such buckling does not occur and $F << F_c$ (Turcotte and Schubert, 2002). For this reason, we do not include the horizontal force as a parameter in our method of flexural modeling (i.e., γ is set to zero and $\xi = \eta = 1$). Thus, Eq. (5) becomes:

$$w(x) = e^{-\frac{x}{\alpha}}\left[C_1\cos\left(\frac{x}{\alpha}\right) + C_2\sin\left(\frac{x}{\alpha}\right)\right] \quad (6)$$

Now, we will present two solutions of Eq. (6) with different boundary conditions as is shown in Fig. 1. In Section 2.1, we rephrase the classic method which uses, as independent parameters, the bending moment M_0 and shear force V_0 at the trench axis (Turcotte and Schubert, 2002; Bry and White, 2007), and the elastic thickness T_e. These three parameters can be constrained using the maximum positive flexure at the apex of the outer rise w_b, and the locations which define the half-width of the fore-bulge $(x_b - x_o)$ (Fig. 1B). In Section 2.2, we present an alternative solution using, as independent parameters, the initial dip of the subducting plate β_0 at the trench axis, the flexure at the trench axis $w(x = 0) = w_0 < 0$ and the elastic thickness T_e (Fig. 1).

2.1. Method 1

In the classic method, the independent parameters are: (1) the bending moment at the trench axis M_0, (2) the shear force at the trench axis V_0, and (3) the elastic thickness T_e. The boundary conditions at the trench axis are (Fig. 1):

$M(x = 0) = M_0 = -D\frac{d^2w}{dx^2}\Big|_{x=0}$ (bending moment M_0 applied at $x = 0$) and $V(x = 0) = -V_0$ (shear force $-V_0$ applied at $x = 0$).

Additionally, the constants are:

$$C_1 = [V_0\alpha\eta + M_0]\frac{\alpha^2}{2D} \quad (7)$$

and

$$C_2 = -M_0\frac{\alpha^2}{2D} \quad (8)$$

or

$$w(x) = \frac{\alpha^2 e^{-\frac{x}{\alpha}}}{2D}\left[-M_0\sin\left(\frac{x}{\alpha}\right) + (V_0\alpha + M_0)\cos\left(\frac{x}{\alpha}\right)\right] \quad (9)$$

V_0 and M_0 cannot be independently measured from the bathymetric data. However, the height of the fore-bulge w_b and the half-width of the fore-bulge $(x_b - x_o)$ can be measured directly from the bathymetric profiles, as is illustrated in Fig. 1B. Therefore, we express the trench profile in terms of these parameters. Following Turcotte and Schubert (2002), we have:

$$x_b - x_o = \alpha\frac{\pi}{4} \quad (10)$$

and

$$w(x) = w_b e^{\frac{\pi}{4}\sqrt{2}} e^{-\frac{\pi}{4}\left(\frac{x-x_o}{x_b-x_o}\right)}\sin\left[\frac{\pi}{4}\left(\frac{x-x_o}{x_b-x_o}\right)\right] = w_b e^{\frac{\pi}{4}\sqrt{2}} e^{-\frac{(x-x_o)}{\alpha}}\sin\left(\frac{x-x_o}{\alpha}\right) \quad (11)$$

Upon measuring x_o and x_b, the flexural wavelength α is determined using (10). Leaving α constant, flexure of oceanic lithosphere $w(x)$ is determined by measuring w_b. Now, we present an illustrative example with plausible values of the following three independent parameters (x_o, T_e, w_b). First, we designate a value for the parameter x_o, from which x_b is calculated using (10) given a value of the second parameter T_e.

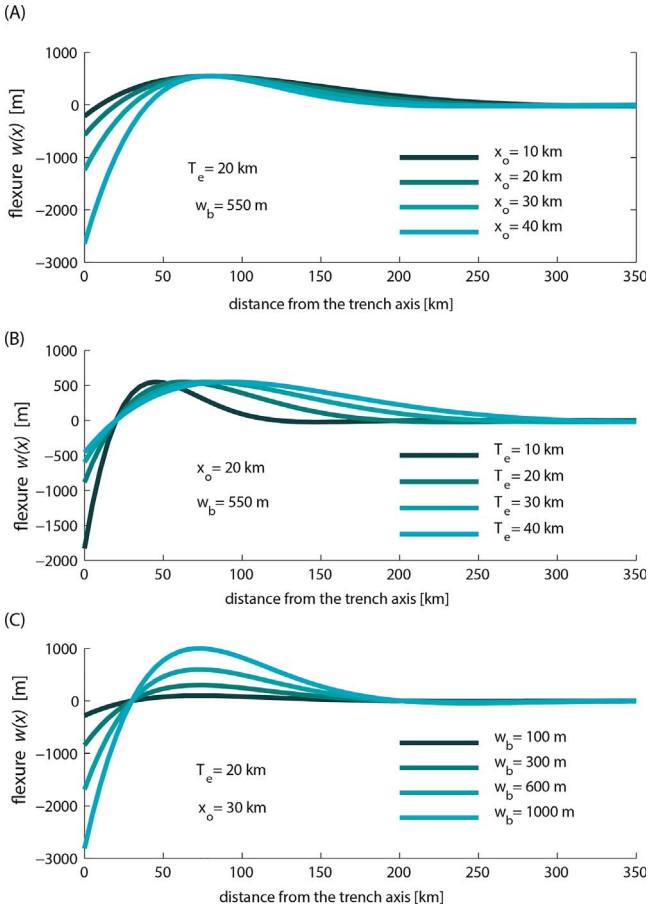

Fig. 2. Flexure of the lithosphere using model 1 (Eq. (11)) for different values of the parameters x_o, T_e, and w_b. (A) x_o controls the flexural amplitude at the trench axis as well as the wavelength of $w(x)$. (B) T_e controls both the flexural amplitude and wavelength. (C) w_b for definition controls the flexural amplitude of the bulge, but it also controls the flexural amplitude at the trench axis.

Elastic thickness is related to the flexural parameter by $T_e = \left(\frac{3\alpha^4 \Delta\rho g (1-\nu^2)}{E}\right)^{1/3}$, thus we will use T_e as the independent parameter instead of α. The third independent parameter w_b is determined using a realistic range of values. Fig. 2 represents an example of how the shape of $w(x)$ can be computed for different values of x_o, T_e, and w_b.

Fig. 2A depicts lithospheric flexure for varying initial values at $x_o = 0$ when T_e and w_b are constant. When x_o is larger, flexural amplitude at the trench axis increases and flexural wavelength decreases. Fig. 2B depicts lithospheric flexure for different values of T_e when x_o and w_b are constant. An increase in T_e results in a longer flexural wavelength as well as a seaward migration of the location of the peak of the outer rise x_b. A second, expected effect is the decrease in the flexural amplitude at the trench axis when T_e increases (more rigid lithosphere). Fig. 2C depicts lithospheric flexure for different values of the height of the fore-bulge w_b when T_e and x_o are constant. An increase in w_b results in a shorter wavelength of $w(x)$ and a greater flexural amplitude at the trench axis. The influence of w_b on $w(x)$ is directly proportional.

In order to quantify the trade-off between the parameters, x_o, T_e and w_b, we calculate a grid mesh for the values of the flexure at the trench axis $w(x = 0) = w_0 < 0$ predicted by Eq. (11) as a function of x_o and T_e for different constant values of w_b (Fig. 3). The results exhibit large amplitudes of the lithospheric flexure at the trench axis when Te is small and x_o is large. This case corresponds to a weak and unstable oceanic lithosphere with a narrow bulge. In contrast, the flexural amplitude at the trench axis decreases when T_e increases and x_o decreases. This case corresponds to a strong, stable oceanic lithosphere with an outer rise characterized by a long wavelength. As a reference, bathymetric profiles published worldwide show that the typical values for w_0 are between 1 and 3 km (e.g., Levitt and Sandwell, 1995; Bry and White, 2007; Contreras-Reyes and Osses, 2010; Zhang et al., 2014; Hunter and Watts, 2016).

2.2. Method 2

In the alternate method, the independent three parameters are the elastic thickness T_e, the initial dip of the subducting plate β_0, and the

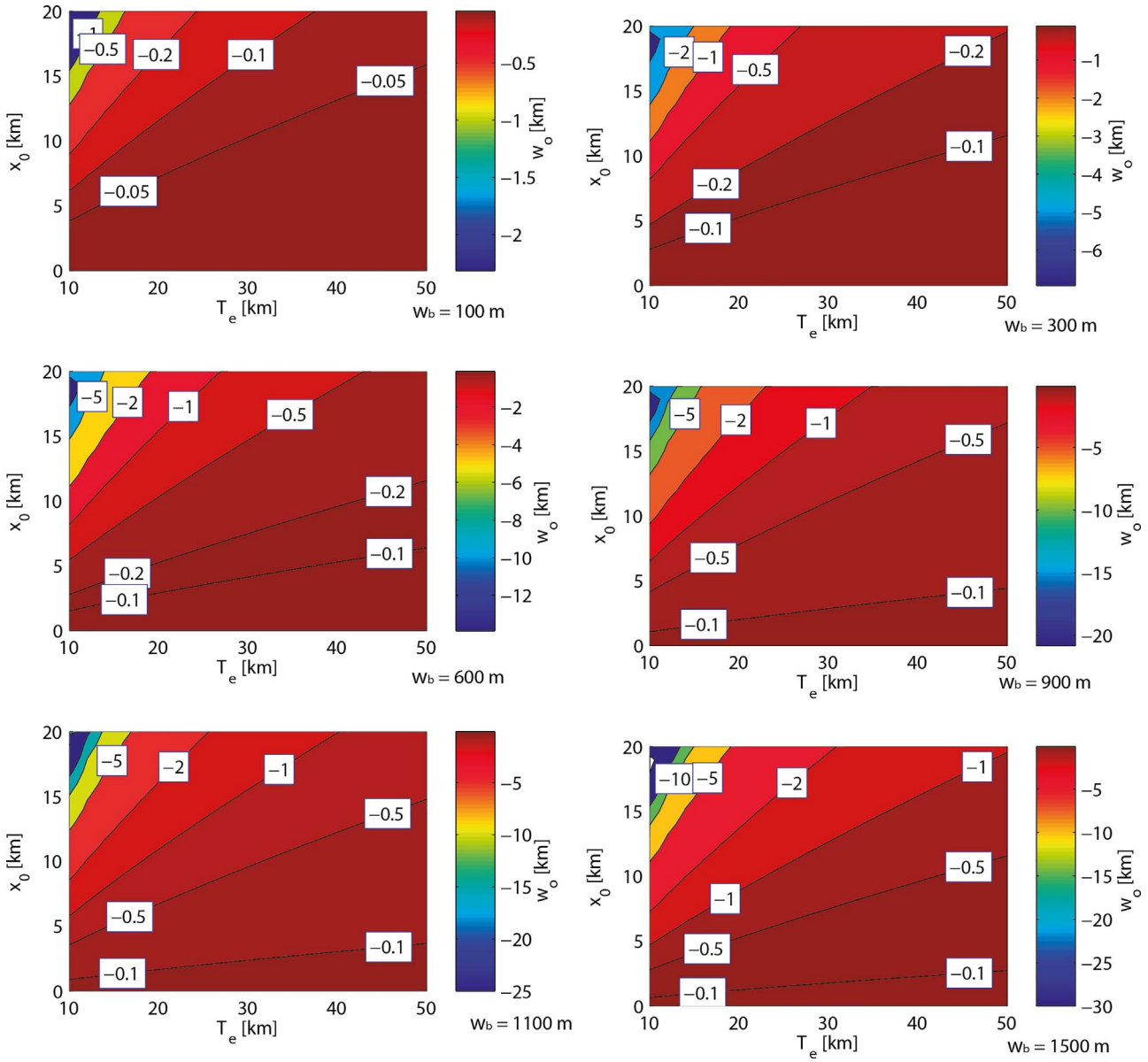

Fig. 3. 2D and contour plots for the flexural amplitude at the trench axis w_0 predicted by the method 1 as a function of the first crossing zero and T_e at different constant values of w_b. The results are shown for different constant values of w_b. Please note that w_0 is directly proportional to w_b (Eq. (11)). As is expected w_0 decreases as the plate becomes stronger for a given value of x_o.

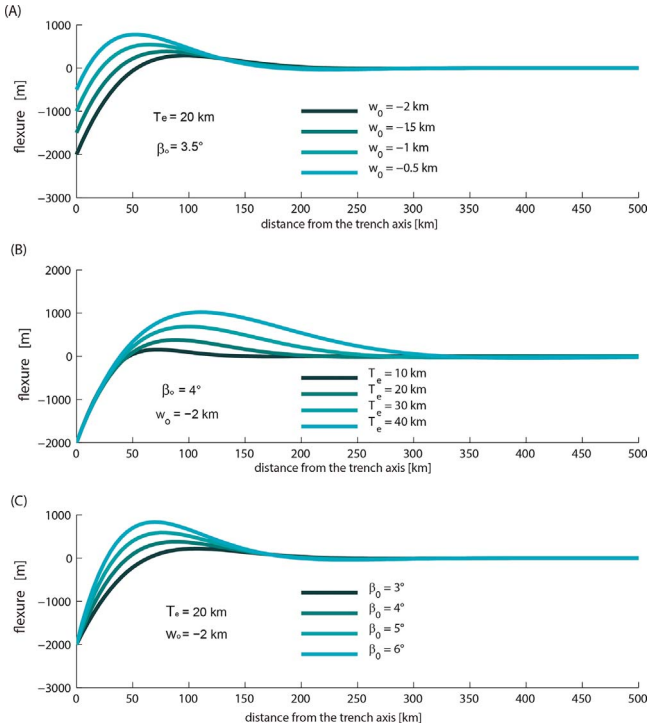

Fig. 4. Flexure of the lithosphere using method 2 (Eq. (12)) for different values of the parameters w_0, T_e, and β_0. (A) w_o is the flexural amplitude at the trench axis and it controls the maximum positive flexural amplitude of $w(x)$. (B) T_e controls both the amplitude and wavelength of $w(x)$. (C) β_0 controls the amplitude of the maximum peak of the outer rise as well as the slope of $w(x)$ along the trench slope.

flexural amplitude at the trench axis w_0 (Fig. 1). For this alternative approach restricted quantities can be directly measured from bathymetric data. The constants C_1 and C_2 of Eq. (6) are derived considering the following boundary conditions:

$$w(x = 0) = w_0$$

and

$$\left.\frac{dw}{dx}\right|_{x=0} = \tan\beta_0$$

Thus, $C_1 = w_0$ and $C_2 = \alpha\tan\beta_0 + w_0$ and the flexure of the lithosphere can be written as:

$$w(x) = e^{-\frac{x}{\alpha}}\left[w_0\cos\left(\frac{x}{\alpha}\right) + (\alpha\tan\beta_0 + w_0)\sin\left(\frac{x}{\alpha}\right)\right] \quad (12)$$

Fig. 4A shows the flexure of the lithosphere for different values of the flexure at the trench axis w_0 with T_e and β_0 constants. The higher the flexural amplitude at the trench axis w_0, the lower the flexural amplitude at the outer rise. Fig. 4B shows the flexure of the lithosphere for different values of T_e with w_0 and β_0 constants. An increase of T_e results in a longer wavelength of $w(x)$ as well as a broader region of high amplitude of $w(x)$ defining a wide and pronounced outer rise. Fig. 2C shows the flexure of the lithosphere for different values of the initial dip of the subducting plate β_0 with T_e and w_0 constants. Results show that plate with high initial dip of subduction present short flexural wavelengths and a high flexural amplitudes at the trench axis. Large values of β_0 also result in the trenchward migration of the peak of the outer rise w_b.

The flexural amplitude is largely sensitive to the values of β_0 (Fig. 4C). For high values of β_0, the model predicts unrealistic values for the height of the fore-bulge and $w(x)$ becomes unstable. However, bathymetric and seismic reflection data do not show evidence of large initial dip values for the subducting plate (e.g., Harris and Chapman, 1994; Maksymowicz, 2015; Hoggard et al., 2017). Instead β_0 is typically a low angle (usually less than 15°), which becomes steeper as the oceanic plate subducts several tens of kilometers (e.g., Contreras-Reyes et al., 2012). Plausible values for β_0 are shown in Fig. 5.

We can calculate the first zero crossing, at $x_1 = 0$ closest to the trench axis, which is predicted by the alternative method using Eq. (12); with the following:

$$x_1 = \alpha a\tan\left(\frac{-w_0}{\alpha\tan\beta_0 + w_0}\right) \quad \text{if } \beta_0 > a\tan\left(\frac{-w_0}{\alpha}\right) \quad (13a)$$

$$x_1 = \frac{\alpha\pi}{2} \quad \text{if } \beta_0 = a\tan\left(\frac{-w_0}{\alpha}\right) \quad (13b)$$

$$x_1 = \alpha\left[a\tan\left(\frac{-w_0}{\alpha\tan\beta_0 + w_0}\right) + \pi\right] \quad \text{if } \beta_0 < a\tan\left(\frac{-w_0}{\alpha}\right) \quad (13c)$$

Parameter sensitivity (w_0, T_e and β_0) for the second model is found by calculating a mesh for the values of the fore-bulge amplitude w_b. The coordinate position of the fore-bulge amplitude x_b can be obtained deriving Eq. (12) and equating to zero, with the following:

$$x_b = \alpha a\tan\left(\frac{\alpha\tan\beta_0}{\alpha\tan\beta_0 + 2w_0}\right) \quad \text{if } \beta_0 > a\tan\left(\frac{-2w_0}{\alpha}\right) \quad (14a)$$

$$x_b = \frac{\alpha\pi}{2} \quad \text{if } \beta_0 = a\tan\left(\frac{-2w_0}{\alpha}\right) \quad (14b)$$

$$x_b = \alpha\left[a\tan\left(\frac{\alpha\tan\beta_0}{\alpha\tan\beta_0 + 2w_0}\right) + \pi\right] \quad \text{if } \beta_0 < a\tan\left(\frac{-2w_0}{\alpha}\right) \quad (14c)$$

Fig. 5 shows a set of meshes for the values of $w(x = x_b) = w_b$ obtained for the second method at different values of T_e, β_0 and w_0. The investigation of T_e vs. β_0 predicts that relatively high values of β_0 and T_e result in large values of w_b. This case correlates with a strong oceanic lithosphere with a steep trench slope angle, and indicates a long bulge and uplifted outer rise. In contrast, low values of β_0 and T_e result in low values of w_b. That is, a weak oceanic lithosphere subducting with a low initial dip (initial flat subduction).

3. Data examples and model testing

We now compare the flexural curves, using methods 1 and 2, with observed bathymetric profile across the Izu-Mariana trench in the western Pacific (Fig. 6). The cross-sectional trench bathymetric profiles were extracted from global bathymetry data sets (Sandwell and Smith, 1997), extending from the approximate trench axis to 500 km seaward of the trench axis. Due to poor sedimentation of the Izu-Mariana trench (e.g., Clift and Vannucchi, 2004), a correction for sediment loading was not applied. In order to reduce the high frequency topographic noise, a median filter was applied to the bathymetric data (2 km moving window). Considering the increase in seafloor depth with age, we extracted the plate age along each profile from the global age grid of Mueller et al. (2008) to correct for the regional topographic tilt. To do so, we compute the depth anomaly, which is the difference between the observed bathymetry, and a theoretical depth given by the age subsidence model of Parsons and Sclater (1977). Each point was corrected as follows:

$$d(t) = 2500 + 350\sqrt{(}t)\,[\text{m}] \quad \text{if } < 20\,\text{Ma}$$

and

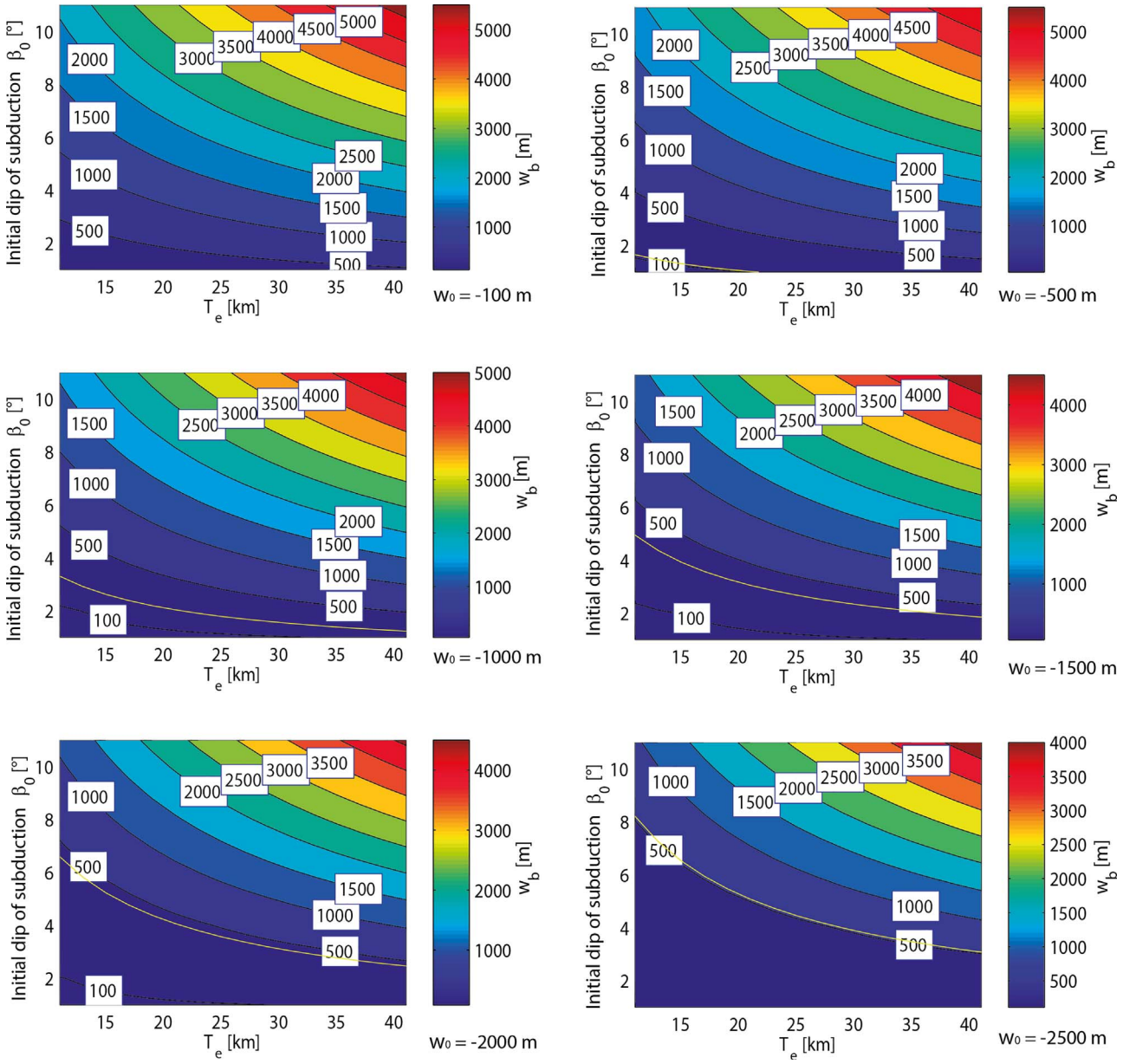

Fig. 5. 2D and contour plots for the height of the forebulge w_b predicted by the method 2 as a function of the initial dip of subduction β_0 and T_e. The results are shown for different constant values of w_0. w_b increases as the plate becomes stronger for a give value β_0. The yellow curve corresponds to the critical curve $a\tan(-2w_0/\alpha)$ according to the set of Eqs. (14a)–(14c). Note that solutions in the domain $\beta_0 > a\tan(-2w_0/\alpha)$ are characterized by high flexural amplitudes and long wavelengths.

$$d(t) = 6400 - 3200e^{-\frac{t}{62.8}}\ [\text{m}] \quad \text{if } t \geq 20\ \text{Ma}$$

The extracted, filtered, and age-corrected profiles were modeled by fitting them to the flexural model using method 1 (Eq. (11)) and the flexural model using method 2 (Eq. (12)), respectively (Fig. 7). The observed profiles clearly illustrate a half-width fore-bulge (x_b, w_b) and an initially crossing at $x_o = 0$, which are depicted by orange and green triangles, respectively. The flexure predicted by method 1 is calculated by measuring the height of the fore-bulge w_b and the elastic thickness T_e (equivalent to measuring x_o and x_b, Eq. (11)). The flexure predicted by method 2 was found by the iteration of T_e and β_0 (w_0 is directly measured from the bathymetric data). The blue curves correspond to the solutions using method 1 for which T_e values are ~24.6 km for the Izu-Bonin trench and ~28 km for the Mariana trench. The calculated T_e values are derived from Eq. (10) by employing respective values for (x_b, w_b) and x_o. Across profile P1, the estimated solutions fit the filtered bathymetric data very well. Across profile P2, the estimated solutions fit the long-wavelength of the bathymetric data well. However, the solution predicted by method 1 fails at the trenchward portion of the bathymetric profile, exhibiting a large misfit in the flexural amplitude at the trench axis (Fig. 7C and D). To quantify the model-error, we calculate the squared RMS (Root Mean Square) error W_{RMS} between the observed bathymetry z_i and the predicted flexure $w_i = w(x_i)$ using:

$$W_{\text{RMS}} = \sqrt{\frac{1}{N}\sum_{i=0}^{N} |w_i - z_i|^2} \tag{15}$$

where N is the number of points along the profiles and w_i is the computed flexure using method 1.

The W_{RMS} values obtained by using method 1 are ~91 m for P1 and

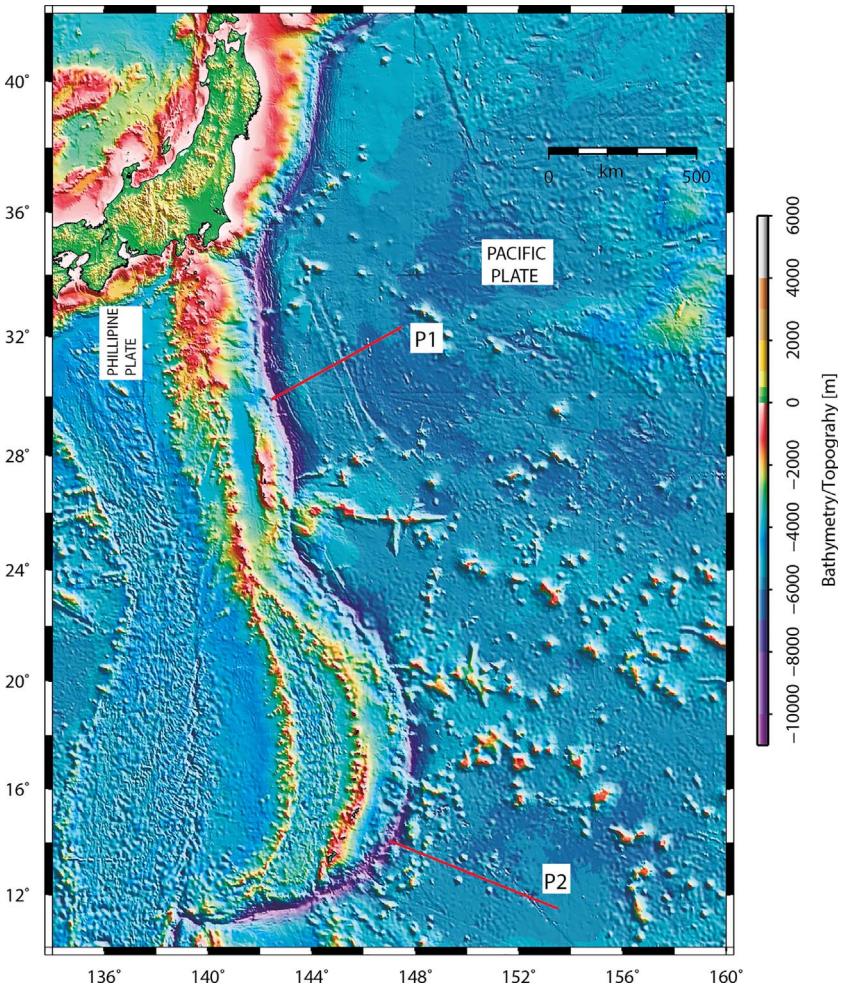

Fig. 6. Bathymetric image of the Izu-Marianas convergent margin in the western Pacific ocean with the location of the bathymetric profiles shown in Fig. 7.

~228 m for P2. The red curves shown in Fig. 7 correspond to the solutions using method 2. Along P1, method 2 appears to fit the bathymetry equally as well, resulting in similar flexural parameters as method 1 (Fig. 7A and B). However, the steepening of the trench slope along P2 results in a large difference in flexural parameters between method 1 and 2. Method 2 predicts a T_e of 40 km with a W_{RMS} value of ~96 m, as opposed to the W_{RMS} value of ~228 m in method 1 (Fig. 7C). The estimated solution obtained by using method 2 fit the trenchward portion of the bathymetric profile well, however, it fails considerably at the seaward part of the outer rise, resulting in a mismatch. The respective W_{RMS} value is about 96 m. In order to illustrate the difference between T_e and β_0, we calculate an alternative solution with $T_e = 30$ km and $\beta_0 = 3.3^\circ$. The resulting flexure is shown in Fig. 7D and it has a W_{RMS} value of ~110 m. In this case, the predicted flexure fits the long wavelength of the bathymetric profile at its seaward portion well. However, the data-misfit increases at the trenchward portion of the bathymetric profile. Both results obtained by using method 2 (Fig. 7C and D) are 50% more accurate than the result obtained using method 1. The range of T_e values obtained using both methods is similar to previous results found by Zhang et al. (2014) across the Mariana trench (19–40 km).

4. Bathymetric data and model parameter uncertainties

The T_e estimates for method 2 presented in the previous section are based simply on the RMS misfit, and it does not explicitly take into account the uncertainty in the bathymetric data. In order to circumvent this problem, we extracted a total of 10 profiles spanning at an interval of 2–5 km along profiles 1 and 2 (Fig. 8A). These ten profiles were stacked together to form a section from which the average bathymetric profile $\overline{z_i}$ and its standard deviation Δz_i were computed (Figs. 8B-C). The next step consists of finding a reference model defined by the parameters T_e and β_0, which is constructed by fitting the average bathymetric profile $\overline{z_i}$. That is, we forward modelled the average bathymetric profiles using (12). Once obtained a reference model, say $\hat{T}_e$ and $\hat{\beta}_0$, these model parameters are perturbed by ± 50%, and the weighted root mean square $W^w_{\mathrm{RMS}}(T_e^j, \beta_0^j)$ is calculated to explore the solution space. A reliable solution is achieved if the computed flexure $w(T_e^j, \beta_0^j)$ reaches the condition $\chi^2 \leq 1$, where χ^2 is given by

$$\chi^2 = \frac{1}{N}\frac{\sum_{j=0}^{N} |w_i(T_e^j, \beta_0^j) - z_i|^2}{\Delta z_i} \tag{16}$$

$\chi^2 = 1$ means that the model error is equal to the bathymetric data uncertainty Δz_i. Figs. 9 and 10 show a 2D grid for the χ^2 parameter as a function of T_e and β_0 for profiles 1 and 2, respectively. The results show that a set of parameters $T_e = 23 \pm 1$ km and $\beta_0 = 5.2 \pm 0.1^\circ$ achieved the condition $\chi^2 \leq 1$ for profile 1. The respective $W^w_{\mathrm{RMS}}(T_e \pm \Delta T_e, \beta_0 \pm \Delta\beta_0)$ is in the range of 75–80 m for profile 1 (Fig. 9). For profile 2, the results show that a set of parameters $T_e = 30 \pm 5$ km and $\beta_0 = 3.7 \pm 0.2^\circ$ achieved the condition $\chi^2 \leq 1$. The respective $W^w_{\mathrm{RMS}}(T_e \pm \Delta T_e, \beta_0 \pm \Delta\beta_0)$ is in the range of 140–150 m

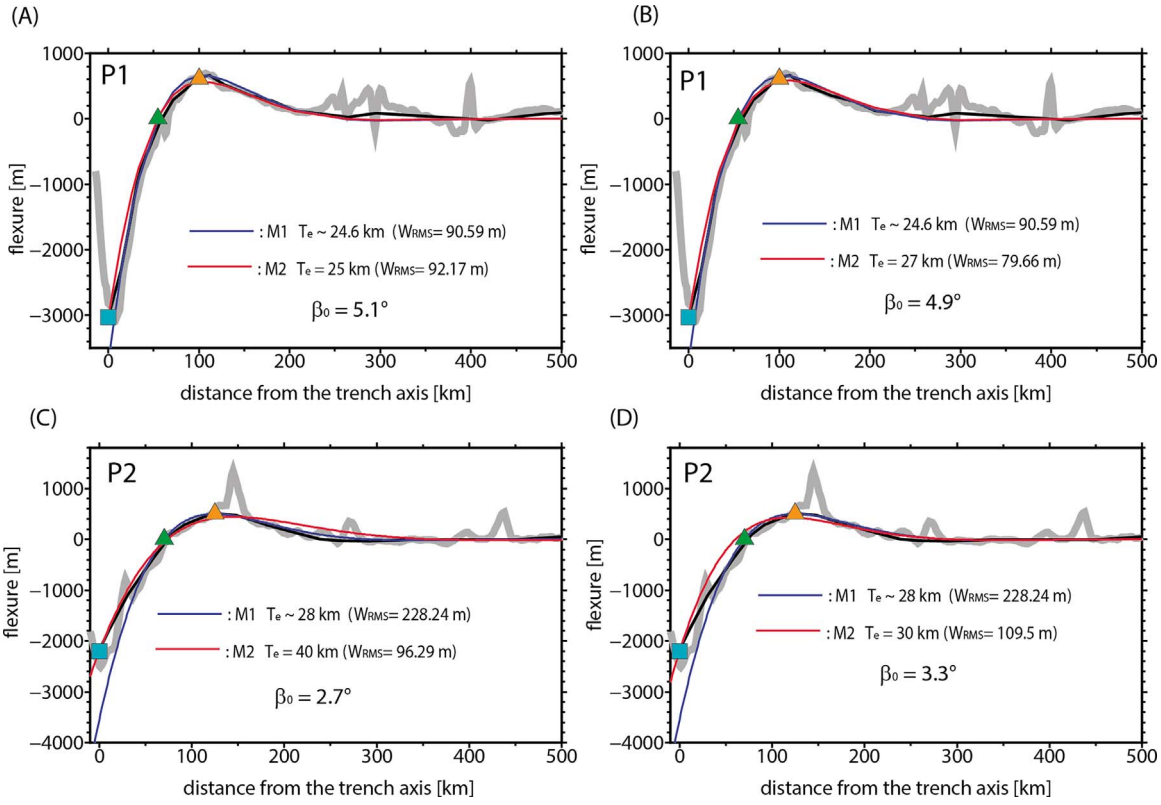

Fig. 7. Flexural parameter values obtained from flexural modeling methods 1 (M1) and 2 (M2). Cyan square, green triangle and orange triangle denote the location of the points $(0, w_0)$, $(x_o, 0)$ and (x_b, w_b), respectively. Grey curve corresponds to the unfiltered bathymetric profiles. The black curve corresponds to the observed bathymetric profile after applying a median filter of 33 points (~2 km window). The bathymetry profiles were fit to formula (11) for method 1 (blue curves) while the data were fit to formula (12) for method 2 (red curves). (A) and (B) trench-normal bathymetric profiles across the Izu-Bonin Trench (P1). (C) and (D) trench-normal bathymetric profiles across the Marianas Trench (P2). The presented squared RMS (Root Mean Square) error W_{RMS} was calculated related to the filtered bathymetric profile.

(Fig. 10). The weighted root mean square $W^{w}_{\mathrm{RMS}}(T_e^j, \beta_0^j)$ is calculated depending on the position x along the profile. Features unrelated to plate flexure like seamounts and spreading center fabric are less weighted.

5. Discussion

The classic approach (method 1, Section 2.1) utilizes morphological information of the trenchward part of the outer rise (specifically, the half-width of the fore-bulge (x_b, w_b)). In general, the outer rise topography presents morphological features related to spreading center fabric, seamounts, and bend faults; as well as other large topographic features that obscure the trench and outer rise signature. These features are not related to the mechanical, long-wavelength flexure of the lithosphere, and can be considered noise. Therefore, a basic requirement to model the flexure of the lithosphere is the clear identification of the fore-bulge to model $w(x)$ using the method 1. However, the precise identification of (x_b, w_b) is often difficult due to increased topographic noise, which is sometimes of the same amplitude as w_b. In which case, method 1 likely provides a poor estimate on the flexural parameters. Nevertheless, method 1 provides a better fit to the data in the seaward portion of the outer rise and to the long wavelength of the $w(x)$ (Fig. 7).

The alternative method (method 2, Section 2.2) requires the morphological information of the trench axis (β_0 and w_0), which is typically more precise to identify than the half-width of the fore-bulge. This is due to the much higher values of w_0 related to w_b (usually more than 5 times; Caldwell et al., 1976; Levitt and Sandwell, 1995). For bathymetric profiles where the fore-bulge is clearly observable, the T_e estimates obtained by using methods 1 and 2 increase in similarity (Fig. 7A and B). In contrast, underdeveloped fore-bulges might result in a large source error when using method 1. Underdeveloped fore-bulges (small outer rise) are usually found in convergent margins where the oceanic subducting plate is young and weak. Examples include the southeastern Gulf of Alaska and southern Chile (Harris and Chapman, 1994; Contreras-Reyes and Osses, 2010). In these cases, visual estimates of (x_b, w_b) are very sensitive to the estimate of T_e and are highly suspect because the classic model may correlate with non-flexural topography (Caldwell et al., 1976; Judge and McNutt, 1991; Harris and Chapman, 1994; Bry and White, 2007). We believe our alternative method is better because w_0 and β_0 are more easily identified from the bathymetric data, mainly due to the high amplitude of w_0.

Plate weakening mechanisms create additional errors when fitting the trenchward portion of the bathymetric profiles. In this region, the oceanic plate exhibits high curvatures and the bending moments, which exceed the yield stress of the oceanic lithosphere causing brittle failure in the upper part of the plate (Fujie et al., 2003; Faccenda, 2014). The inelastic behavior of the oceanic plate has been modeled using yield strength envelopes, which allow any T_e measurement to be converted to the true mechanical thickness (e.g., McAdoo et al., 1978; McNutt and Menard, 1982; Hunter and Watts, 2016). Alternatively, a reduction in T_e has been incorporated to simulate the yielding associated with the decreased strength of the lithosphere towards the trench (i.e., Judge and McNutt, 1991; Contreras-Reyes and Osses, 2010; Hunter and Watts, 2016). Though our extracted bathymetric profile was adequately, analytically fit using methods 1 and 2 (the aim of this paper), the fit could be improved by introducing a variable flexural rigidity or

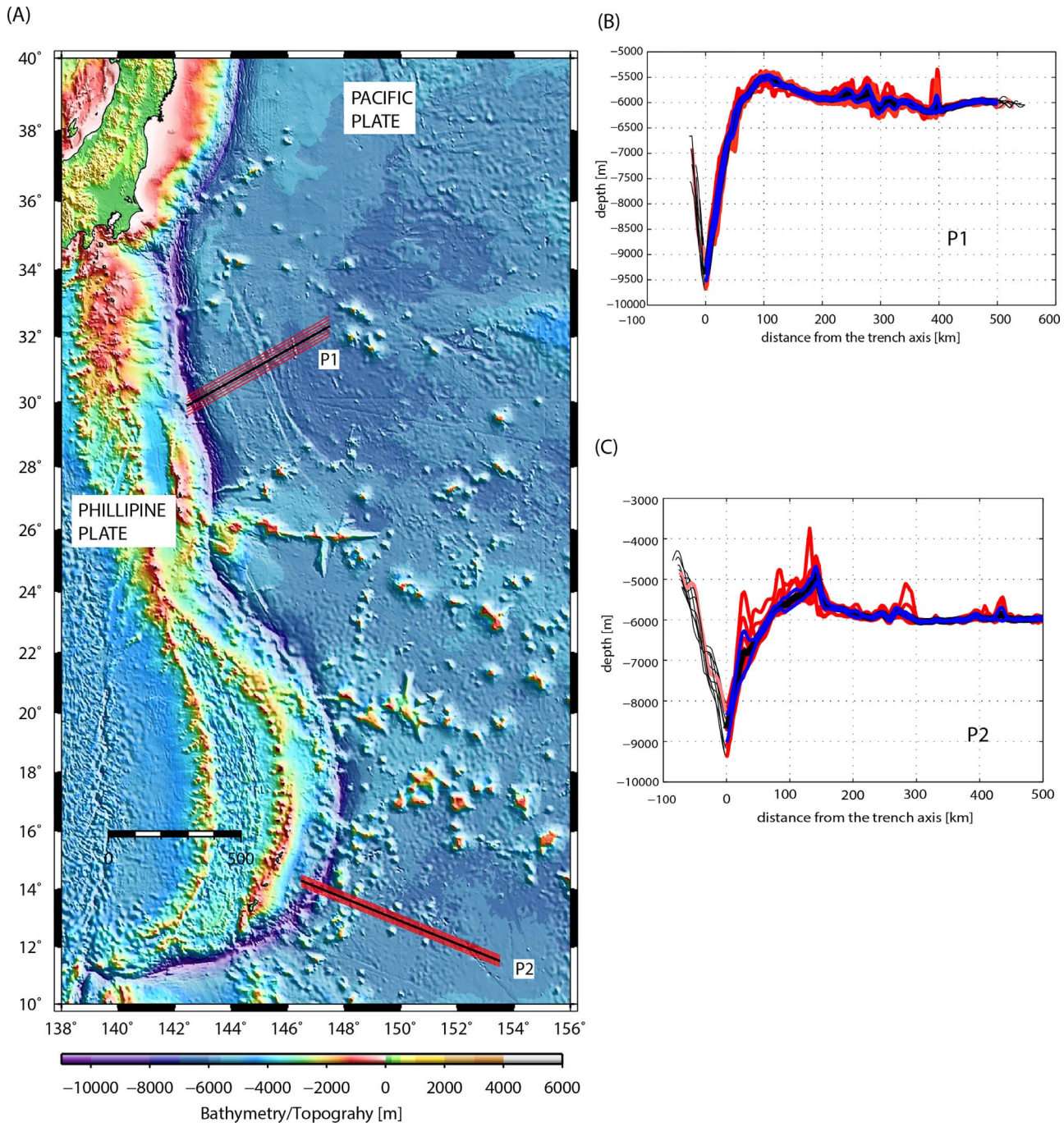

Fig. 8. (A) Bathymetric image of the Izu-Marianas convergent margin in the western Pacific ocean. Basement topography of every ten individual profiles (red lines) was stacked to form an averaged section for modeling and to estimate the bathymetric uncertainties. The extracted bathymetry of these ten individual profiles are shown in (B) and (C) as red curves. (B) and (C) The black curves represent the stacked average bathymetry $\overline{z_i}$, while the blue curves correspond to the bathymetry uncertainties Δz_i for the respective profiles 1 and 2.

variable elastic thickness throughout a given profile. For example, in profile P2 (Fig. 7C), the seaward slope is steeper that the flexure predicted by method 2. By increasing the value of β_0 and decreasing the value of T_e, the seaward slope is adjusted for a better fit, but the trenchward slope of the bulge presents an increased misfit, implying that flexural rigidity is increased as the plate approaches to the trench. Values of constant T_e can be considered weighted averages of the true elastic thickness along the length of the bathymetric profile (Judge and McNutt, 1991). Other general limitations for flexural modeling include interplate stresses, 3D effects (e.g., Manríquez et al., 2014), unbending history and thermal resetting. These conditions cannot be adequately constrained and they mainly depend on unknown factors such as local and regional stress, as well as thermal history (e.g., Levitt and Sandwell, 1995).

Differences in T_e values predicted by methods 1 and 2 along profile P2 (Fig. 7D) can be explained as method 2 aims to find a flexural model with an optimal fit for the trenchward slope, causing the plate to appear stronger. In contrast, method 1 fits well with the long wavelength of the

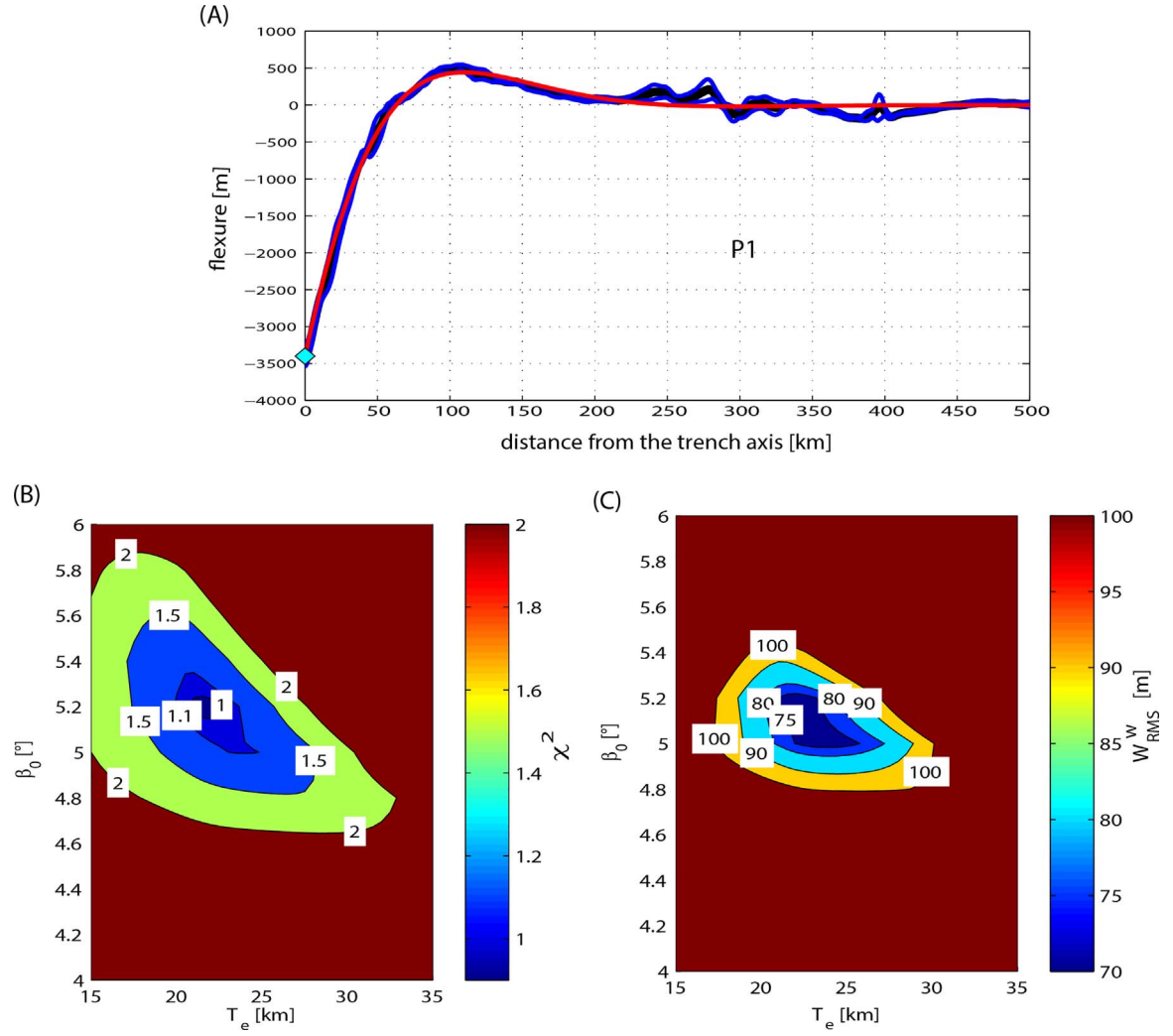

Fig. 9. (A) The black curves represent the stacked average bathymetry $\overline{z_i}$, while the blue curves correspond to the bathymetry uncertainties Δz_i for profile 1 (Fig. 8). The red curve is the calculated flexural model using method 2 that minimizes the weighted W^{w}_{RMS} value. 2D and contour plots for the (B) χ^2 parameter and (C) W^{w}_{RMS} predicted by the method 2 as a function of the initial dip of subduction β_0 and T_e.

flexure seaward of the outer rise, causing the plate to appear weaker. The difference in the estimated T_e is reduced when β_0 is increased, however, the W_{RMS} increases in the trenchward part of the outer rise. This is illustrated in the example shown in Figs. 8–10 by comparing the results of profiles P1 and P2. The bathymetric uncertainty along the trench slope of profile P2 is much higher than along profile P1 (Fig. 8B and C). Consequently, the estimated uncertainties for T_e for profile P2 are up to 5 times higher than along profile P1 (Figs. 9 and 10).

6. Conclusions

In this study, we investigated the mutual dependence of the flexural parameters to model the flexural response of the oceanic lithosphere to loading at trenches using two different analytical solutions. Method 1 corresponds to the classic approach and is limited to parameters x_b, w_b, T_e while the alternative method is limited to parameters w_0, β_0, T_e. This work leads to the following conclusions:

- We find that method 1 is not an accurate estimate of elastic thickness for bathymetric profiles where the outer rise is obscured by topographic noise. In this case, the model may correlate with nonflexural topography. In contrast, when the bulge is well developed and when there is less topographic noise around the outer bulge, the estimated T_e values using methods 1 and 2 become similar.
- The alternative method 2 results in a practical approach when the location of the trench axis is clearly identifiable, regardless of the topographic noise surrounding the outer rise. This method is very sensitive to the initial dip of subduction and it becomes unstable for high values of β_0. Nonetheless, seismic constraints do not show evidence for steep subduction near the trench ($< 15°$), and the alternative plate flexural model provides a smooth fit to the observations. This method predicts large flexural bulges for high β_0 values.
- In general, the validity of the flexural modeling technique for the inversion of the flexural parameters is greatly limited by the presence of short- and long-wavelength bathymetric noise (Levitt and Sandwell, 1995) as well as weakening mechanisms of the oceanic plate related to remnant thermal stress, unbending history, and/or interplate stress (Judge and McNutt, 1991; Contreras-Reyes and Osses, 2010; Hunter and Watts, 2016).

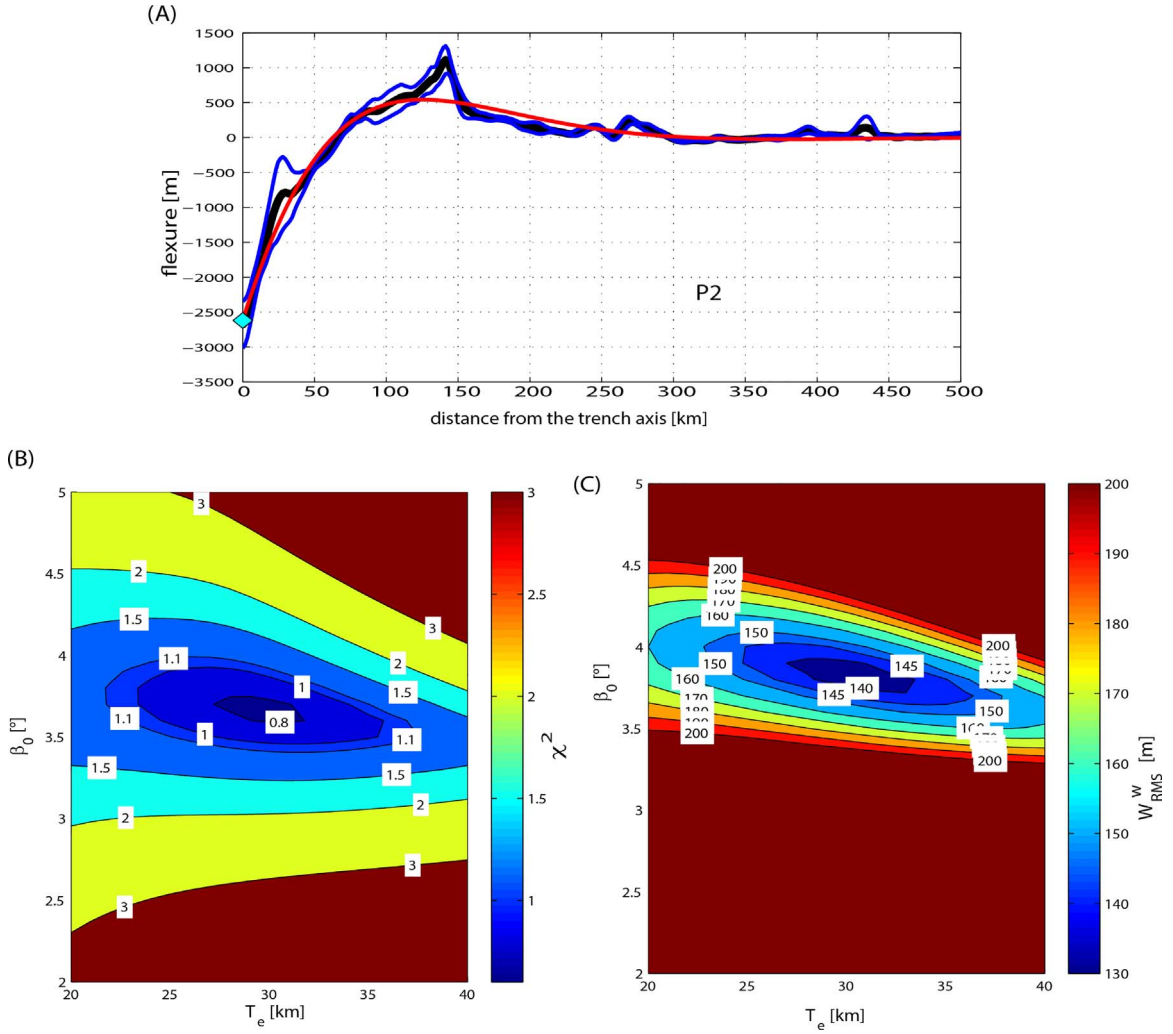

Fig. 10. (A) The black curves represent the stacked average bathymetry $\overline{z_i}$, while the blue curves correspond to the bathymetry uncertainties Δz_i for profile 2 (Fig. 8). The red curve is the calculated flexural model using method 2 that minimizes the weighted W^w_{RMS} value. 2D and contour plots for the (B) χ^2 parameter and (C) W^w_{RMS} predicted by the method 2 as a function of the initial dip of subduction β_0 and T_e.

Acknowledgments

Eduardo Contreras-Reyes acknowledges the support of the Chilean Fondo Nacional de Desarrollo Científico y Tecnológico (FONDECYT), Grant 1170009. Jeremías thanks the support of Master Becas CONICYT. The authors than Mikenna Montgomery for comments on the English. We thank the Editor Irina Artemieva and an anonymous reviewer for their constructive reviews of the manuscript.

References

Bry, M., White, N., 2007. Reappraising elastic thickness variation at oceanic trenches. J. Geophys. Res. 112, B08414. http://dx.doi.org/10.1029/2005JB004190.
Billen, M.I., Gurnis, M., 2005. Constraints on subducting plate strength within the Kermadec trench. J. Geophys. Res. 110, B05407. http://dx.doi.org/10.1029/2004JB003308.
Bodine, J.H., Watts, A.B., 1979. On the lithospheric flexure seaward of the Bonin and Mariana Trenches. Earth Planet. Sci. Lett. 43, 132–148.
Bodine, J.H., Steckler, M.S., Watts, A.B., 1981. Observations of flexure and the rheology of the oceanic lithosphere. J. Geophys. Res. 86 (B5), 3695–3707.
Caldwell, J.G., Haxby, W.F., Karig, D.E., Turcotte, D.L., 1976. On the applicability of a universal elastic trench profile. Earth Planet. Sci. Lett. 31, 239–246.
Capitanio, F.A., Morra, G., Goes, S., 2009. Dynamics of plate bending at the trench and slabplate coupling. Geochem. Geophys. Geosyst. 10, Q04002. http://dx.doi.org/10.1029/2008GC002348.
Christensen, D.H., Ruff, L.J., 1988. Seismic coupling and outer rise earthquakes. J. Geophys. Res. 93 (B11), 13421–13444.
Clift, P., Vannucchi, P., 2004. Controls on tectonic accretion versus erosion in subduction zones: implications for the origin and recycling of the continental crust. Rev. Geophys. 42, RG2001. http://dx.doi.org/10.1029/2003RG000127.
Conrad, C., Lithgow-Bertelloni, C., 2002. How mantle slabs drive plate tectonics. Science 298 (5591), 207–209.
Contreras-Reyes, E., Osses, A.L., 2010. Lithospheric flexure modelling seaward of the Chile trench: implications for oceanic plate weakening in the Trench Outer Rise region. Geophys. J. Int. 182, 97–112.
Contreras-Reyes, E., Jara, J., Grevemeyer, I., Ruiz, S., Carrizo, D., 2012. Abrupt change in the dip of the subducting plate beneath north Chile. Nat. Geosci. 5, 342–345. http://dx.doi.org/10.1038/ngeo1447.
Faccenda, M., 2014. Water in the slab: a trilogy. Tectonophysics 614, 1–30. http://dx.doi.org/10.1016/j.tecto.2013.12.020.
Forsyth, D., Uyeda, S., 1975. On the relative importance of the driving forces of plate motion. Geophys. J. Int. 43 (1), 163–200. http://dx.doi.org/10.1111/j.1365-246X.1975.tb00631.x.
Fujie, G., Kodaira, S., Yamashita, M., Sato, T., Takahashi, T., Takahashi, N., 2003. Systematic changes in the incoming plate structure at the Kuril trench. Geophys. Res. Lett. 40, 88–93. http://dx.doi.org/10.1029/2012GL054340.
Harris, R., Chapman, D., 1994. A comparison of mechanical thickness estimates from trough and seamount loading in the southeastern Gulf of Alaska. J. Geophys. Res. 99 (B5), 9297–9317.
Hoggard, M., Winterbourne, J., Czarnota, K., White, N., 2017. Oceanic residual depth measurements, the plate cooling model, and global dynamic topography. J. Geophys. Res. http://dx.doi.org/10.1002/2016JB013457.
Hunter, J., Watts, A.B., 2016. Gravity anomalies, flexure and mantle rheology seaward of circum-Pacific trenches. Geophys. J. Int. 207, 288–316.
Judge, A.V., McNutt, M.K., 1991. The relationship between plate curvature and elastic plate thickness: a study of the Peru-Chile Trench. J. Geophys. Res. 96 (B10), 16625–16639.
Levitt, D.A., Sandwell, D.T., 1995. Lithospheric bending at subduction zones based on depth soundings and satellite gravity. J. Geophys. Res. 100, 379–400.
Maksymowicz, A., 2015. The geometry of the Chilean continental wedge: tectonic

segmentation of subduction processes off Chile. Tectonophysics 659, 183–196. http://dx.doi.org/10.1016/j.tecto.2015.08.007.
Manríquez, P., Contreras-Reyes, E., Osses, A., 2014. Lithospheric 3-D flexure modelling of the oceanic plate seaward of the trench using variable elastic thickness. Geophys. J. Int. 196 (2), 681–693.
Masson, D.G., 1991. Fault patterns at outer trench walls. Mar. Geophys. Res. 13 (3), 209–225.
McAdoo, D.C., Martin, C.F., Poulose, S., 1985. Seasat observations of flexure: evidence for a strong lithosphere. Tectonophysics 116, 209–222.
McAdoo, D.C., Caldwell, J.G., Turcotte, D.L., 1978. On the elastic-perfectly plastic bending of the lithosphere under generalized loading with application to the Kuril Trench. Geophys. J. R. Astron. Soc. 54, 11–26.
McNutt, M.K., Menard, H.W., 1982. Constraints on yield strength in the oceanic lithosphere derived from observations of flexure. Geophys. J. R. Astron. Soc. 71, 363–394.
Mueller, R.D., Sdrolias, M., Gaina, C., Roest, W.R., 2008. Age, spreading rates and spreading symmetry of the world's ocean crust. Geochem. Geophys. Geosyst. 9, Q04006. http://dx.doi.org/10.1029/2007GC001743.
Mueller, S., Phillips, R.J., 1995. On the reliability of lithospheric constraints derived from models of outer-rise flexure. Geophys. J. Int. 123 (3), 887–902.
Parsons, B., Molnar, P., 1978. The origin of outer topographic rises associated with trenches. Geophys. J. Int. 1 (4), 707–712.
Parsons, B., Sclater, J.G., 1977. An analysis of the variation of ocean floor bathymetry and heat flow with age. J. Geophys. Res. 82 (5), 803–827.
Ruiz, J., Contreras-Reyes, E., 2015. Outer rise seismicity boosted by the Maule 2010 Mw 8.8 megathrust earthquake. Tectonophysics 653, 127–139.
Sandwell, D.T., Smith, W.H.F., 1997. Marine gravity anomaly from Geosat and ERS-1 satellite altimetry. J. Geophys. Res. 102, 10039–10054.
Turcotte, D.L., McAdoo, D.C., Caldwell, J.G., 1978. An elastic-perfectly plastic analysis of the bending of the lithosphere at a trench. Tectonophysics 47, 193–208.
Turcotte, D., Schubert, G., 2002. Geodynamics—Applications of Continuum Physics to Geological Problems, 3rd ed. Cambridge University Press ISBN: 9780521666244.
von Huene, R., Scholl, D.W., 1991. Observations at convergent margins concerning sediment subduction, subduction erosion, and the growth of continental crust. Rev. Geophys. 29 (3), 279–316. http://dx.doi.org/10.1029/90JB00230.
Watts, A.B., Talwani, M., 1974. Gravity anomalies seaward of deep-sea trenches and their tectonic implications. J. R. Astron. Soc. 36, 57–92.
Watts, A.B., 2001. Isostasy and Flexure of the Lithosphere. Cambridge Univ. Press, New York, pp. 6325–6345 458pp.
Zhang, F., Lin, J., Zhan, W., 2014. Variations in oceanic plate bending along the Mariana trench. Earth Planet. Sci. Lett. 401, 206–214.